energies

MDPI

Article

Fuel Cell-Based Inductive Power Transfer System for Supercapacitor Constant Current Charging

Nicola Campagna [1,*,†], Vincenzo Castiglia [1,†], Francesco Gennaro [2], Angelo Alberto Messina [2] and Rosario Miceli [1]

[1] Department of Engineering, University of Palermo, 90128 Palermo, Italy; vincenzo.castiglia@unipa.it (V.C.); rosario.miceli@unipa.it (R.M.)
[2] ST Microelectronics, 95121 Catania, Italy; francesco.gennaro@st.com (F.G.); angelo.messina@st.com (A.A.M.)
* Correspondence: nicola.campagna@unipa.it; Tel.: +39-329-8935-951
† These authors contributed equally to this work.

Abstract: The majority of urban CO_2 emissions come from the transportation sector. To be able to reduce them, it is definitely necessary to replace Internal Combustion Engine (ICE) vehicles with electric ones. In this article, a public transport system is proposed, consisting of a supercapacitor (SC)-powered electric vehicle (EV) charged through a fuel cell-powered (FC) Inductive Power Transfer (IPT) system. The bus runs the usual route and it is charged each time it reaches the terminal, where the charging system is placed. The main advantages of the proposed system are related to the long-term cost of the EV, compared to a classic battery-powered system, to the aspects of ease of use and safety for charging operations and to the possibility of realizing a net-zero-energy transport system thanks to the use of green hydrogen. In addition, the proposed charging methodology allows for better energy utilization avoiding major changes to the main power grid. In this article, the system is presented considering a real case study; it is simulated at system and hardware level, and then validated through the realization of a scaled-down prototype.

Keywords: supercapacitor (SC); fuel cell (FC); energy storage; wireless power transfer (WPT); electric vehicles (EVs)

Citation: Campagna, N.; Castiglia, V.; Gennaro, F.; Messina, A.A.; Miceli, R. Fuel Cell-Based Inductive Power Transfer System for Supercapacitor Constant Current Charging. *Energies* **2024**, *17*, 3575. https://doi.org/10.3390/en17143575

Academic Editor: Abdul-Ghani Olabi

Received: 12 June 2024
Revised: 12 July 2024
Accepted: 17 July 2024
Published: 20 July 2024

1. Introduction

Energy transition poses numerous challenges in responding to the need for CO_2 emission reduction [1]. Especially in big cities, most of the CO_2 emissions are related to both private and public mobility. For this reason, the automotive research field is called upon to provide the best solutions to the urban pollution problems related to transportation.

Nowadays, public transportation is mainly based on Internal Combustion Engine (ICE) bus fleets, although the use of natural gas-powered buses is increasing, while widespread use of electric buses is struggling to take off. This is mainly due to electric energy storage issues [2]. Among the different storage technologies employed in automotive vehicles, the most commonly used is the electrochemical one through batteries, especially Li-ion ones. Even though it is a mature technology, the cost of such storage systems can reach 30% of the vehicle total cost [3]. This makes the cost of replacing an ICE bus fleet with a full electric one unsustainable. In addition, the electric bus fleet charging would mainly take place at night [4]. This means that the energy for the recharging operation would be almost entirely produced from non-renewable sources, in addition to a heavy overload for the main grid represented by numerous fleets being charged contemporaneously.

An alternative solution to batteries could be the use of supercapacitors (SCs). The latter are characterized by high capacitance values, fast response times and high power density [5]. More importantly, they have a long operating life and they can be charged and discharged approximately one million times [6]. The main drawback of SCs is the lower energy density compared to batteries, making them ineffective as storage devices

for passenger vehicles. A review of the available scientific literature reveals that there are relatively few studies exploring the potential of supercapacitors as the primary energy source for vehicles. Current research efforts primarily focus on hybrid systems that combine supercapacitors with batteries, leveraging the strengths of both technologies. In refs. [7–9], SCs are employed in a Hybrid Energy Storage System with the aim of preserving the battery life, whereas in ref. [10] SCs are used to assist the regenerative braking. However, considering the routes for urban transport buses, the short loop routes and frequent stops can be exploited to use SCs as a unique on-board storage source. In fact, SCs can be designed for the energy requirement of the short loop route and recharged in a short time, during the bus stop. This article has the aim of investigating the feasibility of SC-powered buses, in conjunction with the design of a proper charging system.

Different EV charging infrastructures can be chosen. They can be classified into three categories: swapping, wired and wireless [11]. Swapping consists of the on-the-fly replacement of the discharged storage with a charged one but it is impractical for large vehicles. Wired systems are the most common and involve the use of cables to connect the vehicle to the charging station. Wireless systems are the most recent; the lack of physical connections makes them user-friendly and safer. Among the different types of wireless charging systems, the Resonant Inductive Power Transfer (RIPT) ones are the most commonly used because of the high power levels reachable. The energy transfer takes place thanks to the inductive coupling between two coils: one, called primary, which acts as a transmitter, positioned below the road surface, and a secondary one, which acts as a receiver, positioned on the vehicle chassis [12]. In the literature, there are numerous examples that show the benefits of wireless vehicle charging [13–15]. Among these, WPT enables the possibility of recharging vehicles on the road, during their ordinary travel through dynamic systems [16,17]. However, these systems require the implementation of vehicle detection strategies for charging optimization, thus the implementation of complex Foreign Object Detection algorithms as shown in refs. [18,19] and the need for complex control strategies [20]. Moreover, in the case of urban public transport, the transition from an ICE-based transport system to a fully electric one requires significant economic investments for the installation of the charging infrastructure in the city. For this reason, a static WPT charging system is chosen as a charging possibility in this work.

In order to significantly reduce CO_2 urban emissions, the energy required for the vehicles charging should be produced from renewable sources. In the specific case of a public transport charging station, the most immediate solution is to build a photovoltaic shelter that can generate the electricity for charging. However, the variability and fluctuation in energy production are one of the major challenges associated with renewable energy. A potential solution to the intermittency of the solar source is the use of hydrogen through fuel cells. These are electrochemical devices that can generate electricity from hydrogen and water. Hydrogen can be produced on site from an electrolyzer. The benefits of integrating an electrolyzer into the electricity grid to support renewable energy are widely demonstrated in refs. [21,22]. An additional solution is represented by the transport of hydrogen in city gas pipelines, allowed according to European Directive 2021/2168. For these reasons, this paper examines the power supply of the charging system through a fuel cell. Overall, this work aims to investigate the feasibility of using SC-powered buses for urban public transport, highlighting the benefits of charging at bus terminals rather than overnight charging at depots and comparing this scenario with traditional batteries. In particular, this work will analyze the energy consumption of SC-powered buses under real driving conditions and a brief technical and economic feasibility study of implementing SC-powered buses in a real-world urban public transport system is provided. Moreover, an additional goal of the work is to provide a possible solution for the design of a net-zero-carbon charging station in which a WPT charging system is powered by a fuel cell.

In Section 2, the proposed system description and design are provided; in Sections 3 and 4, the system-level simulation and the hardware-level simulation are respectively presented.

In Section 5, the experimental validation is carried out through a scaled-down prototype and in Section 6 a technical–economical analysis is provided. In Figure 1, a graphical representation of the work structure is shown to improve the readability of the work.

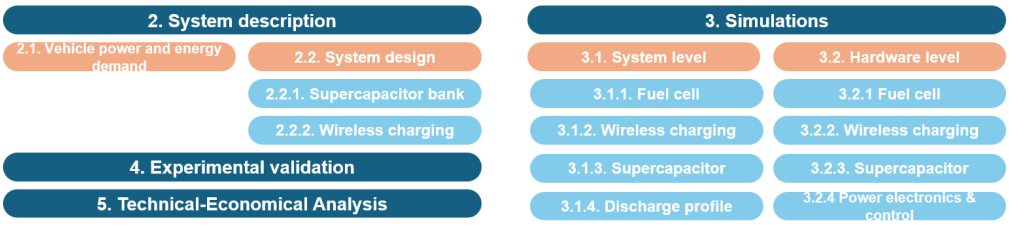

Figure 1. Graphical representation of the article structure.

2. System Description

In Figure 2, a functional representation of the proposed system is provided. The system is composed of a SC-powered shuttle bus and a recharging station. The latter is placed at the bus terminal, employing a FC-based IPT recharging system which provides the required energy for the loop route run. Hydrogen storage feeds the FC, which supplies the IPT transmitter side. On the shuttle bus, the IPT receiver side picks up the transmitter transferred energy to recharge the vehicle storage system, represented by a SC bank. For simplicity, this paper presents only a single bus line, and therefore a single terminal where the bus is recharged. Extending the analysis conducted in this work to the entire urban transport system of a city, it is necessary to guarantee the redundancy of the charging stations. In particular, two conditions must be satisfied:

- Each bus line must always have at least two charging station terminals on its route;
- A charging station must be shared by at least two bus lines.

In case of the failure of a charging station, the remaining stations must be able to handle the entire bus fleet. This means that the number of charging stations should be greater than or equal to the number of buses in the fleet, plus an additional safety factor. To meet these conditions, it is necessary to carefully plan the location of the charging stations. The stations should be evenly distributed along the bus route, taking into account the traffic patterns and the expected demand for bus services.

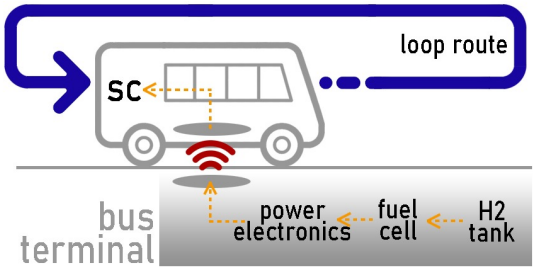

Figure 2. Functional representation of the proposed system.

The architecture of a charging station is shown in Figure 3. The FC voltage is regulated with a DC/DC boost converter; then, a DC/AC inverter provides the high-frequency AC voltage needed for the magnetic coupling of the IPT system. To recharge the SC bank, the constant current method is used; therefore, an AC/DC rectifier is interposed between the IPT receiver and the SC bank. The SC recharging current is controlled acting on the primary side inverter, as it will be described in Section 3.2.4. In order to validate this system, the criteria for sizing the components and the system design are presented in the following paragraphs and sections. In particular, the validation is conducted on a laboratory-scale prototype. Specifically, the characteristics of the chosen components are reported in the following sections.

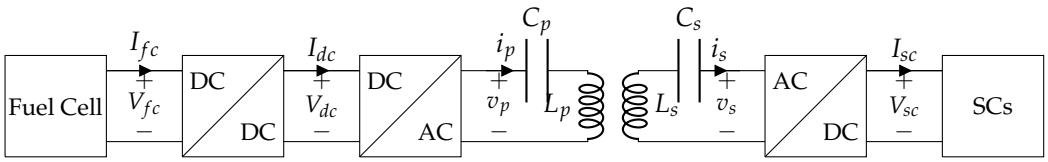

Figure 3. Block diagram of the FC-IPT system.

2.1. Vehicle Power and Energy Demand

For the implementation of the vehicle SC power system, a loop route of a shuttle bus serving the Palermo University Campus was examined. The route has a length of 3.2 km and nine stops have been positioned at the focal points of the campus as reported in Figure 4. The lengths of the sections between the stops are shown in Table 1. Through a redundant acquisition system consisting of an accelerometer, a speedometer and a GPS tracker, the altimetric profile and the speed profile of a vehicle traveling along the considered route were measured, taking into account a stop time equal to 30 s. The acquired speed profile and altimetric profile are reported in Figure 5, together with the road slope angle trend.

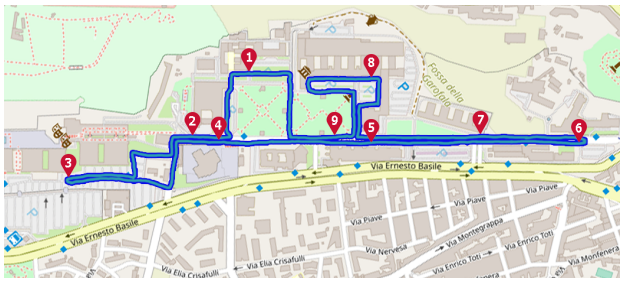

Figure 4. Loop shuttle bus route.

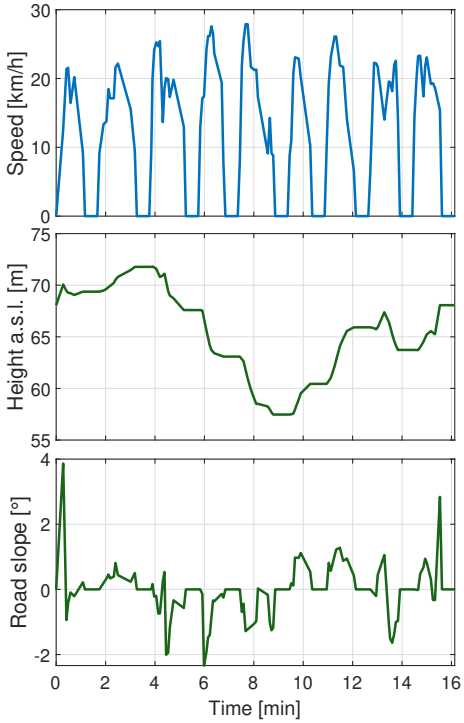

Figure 5. Loop shuttle bus route specifications: speed profile, altimetric profile and road slope angle trend.

Table 1. Route stretch lengths.

1–2	0.2	km	6–7	0.2	km
2–3	0.3	km	7–8	0.4	km
3–4	0.5	km	8–9	0.4	km
4–5	0.3	km	9–1	0.4	km
5–6	0.5	km			

A fully electric shuttle bus, whose characteristics are reported in Table 2, was considered.

Table 2. Shuttle bus characteristics.

Max total passengers	22	-
Passenger weight	1540	kg
Motor power	135	kW
Maximum torque	290	Nm
Li-ion battery capacity	44	kWh
Frontal area	5.78	m^2
Gross weight	5000	kg

The vehicle dynamic model was implemented in the Simulink 2019 environment to calculate the power required and the total energy consumption. The simulation output data were employed for the SC supply system sizing. The total power P_{tot} can be calculated as the product of the total road load F_{tot} and the vehicle speed v_v as reported in (1).

$$P_{tot} = F_{tot} \cdot v_v. \tag{1}$$

The total energy consumption E_{tot} can be calculated by integrating the total power over time for the whole duration of the cycle as in (2).

$$E_{tot} = \int P_{tot} dt. \tag{2}$$

The total road load F_{tot} is calculated as the sum of the motion force F_i (according simply to Newton's second law), the road slope force F_s, the road load friction F_r and the aerodynamic drag force F_a as reported in (3).

$$F_{tot} = F_i + F_s + F_r + F_a. \tag{3}$$

Each single contribution can be evaluated as reported in (4)–(7):

$$F_i = m_v \cdot a_v, \tag{4}$$

$$F_s = m_v \cdot g \cdot sin(\alpha_s), \tag{5}$$

$$F_r = m_v \cdot g \cdot c_{rr} \cdot cos(\alpha_s), \tag{6}$$

$$F_a = \frac{1}{2} \cdot \rho \cdot c_d \cdot A \cdot v_v^2, \tag{7}$$

in which m_v is the vehicle mass considered as the sum of the gross vehicle mass and the passenger mass; a_v is the vehicle acceleration calculated as the derivative of the speed profile; g is the gravitational acceleration; a_s is the road slope angle; c_{rr} is the road rolling resistance coefficient; ρ is the air density; c_d is the air drag coefficient and A is the vehicle frontal area. In Table 3, the values of each parameter are reported.

The obtained output power profile was then divided by a coefficient equal to 0.95 in order to take into account the power drive system efficiency and a base power equal to

2 kW was added to the entire profile in order to consider the auxiliary system consumption, as shown in Figure 6. In addition, it was checked that the maximum torque required was lower than the motor maximum torque. In Figure 6, the cycle energy is also shown. In particular, the total energy can be considered as the sum of the acceleration energy and the breaking energy.

Table 3. Vehicle dynamic model parameters.

m_v [kg]	g $\left[\frac{m}{s^2}\right]$	c_{rr} [−]	ρ $\left[\frac{kg}{m^3}\right]$	c_d [−]	A [m^2]
6540	9.8	0.011	1.202	0.36	5.78

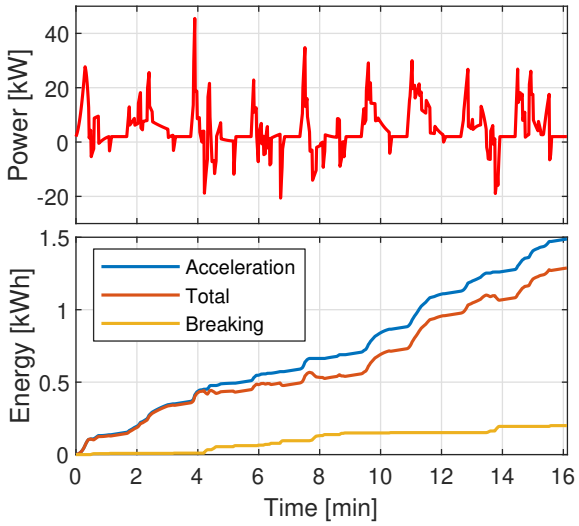

Figure 6. Vehicle power and energy requirement.

2.2. System Design

Once the vehicle power and energy demand are obtained, the on-board storage and Wireless Power Transfer system are properly sized, following the criteria described in the next two subsections.

2.2.1. SC Design

The SC supply system sizing is carried out taking into account the possibility of regenerative braking. For this reason, the total energy is considered. This is equal to 1.28 kWh. For the SC bank sizing, it is increased cautiously by a factor equal to 10%. Then, the effective rating energy E_{cycle} is equal to 1.4 kWh. The maximum current of the cycle $I_{cycle,M}$ is equal to 113.75 A. An important feature of the SC is the ability to store, at the same voltage, more energy than the standard capacitor [5]. The stored energy function of the cell voltage, for a 100 F, 2.7 V SC and for a fictitious traditional capacitor with the same characteristics are shown in Figure 7. This behavior is due to non-linearity because of the presence of the voltage-dependent capacitor in the first branch. Figure 7 also shows the ratio between the SC stored energy and a standard capacitor stored energy:

$$K_e(V) = \frac{E_{sc}(V)}{E_c(V)}, \tag{8}$$

in which

$$E_{sc}(V) = \int_0^{t_{charge}} P_{sc} dt, \tag{9}$$

$$E_c(V) = \frac{1}{2} C \cdot V^2. \tag{10}$$

Therefore, the effective cell energy E_{cell}, considering discharging the cell from the maximum voltage to half the maximum voltage, is calculated as follows:

$$E_{cell} = \frac{1}{2}C\left[V_{cell,M}^2 - \left(\frac{V_{cell,M}}{2}\right)^2\right]\frac{K_e(V_{cell,M})}{3600}. \quad (11)$$

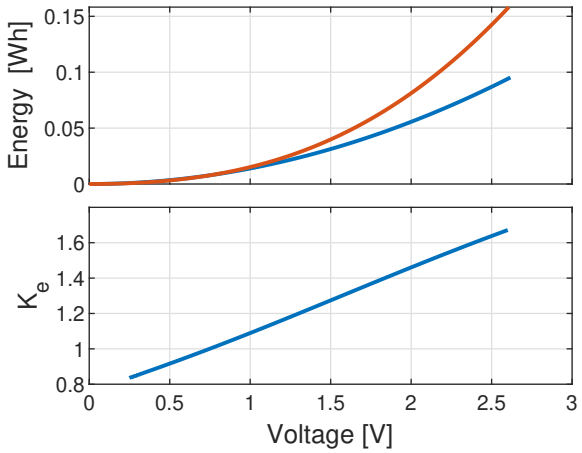

Figure 7. Comparison of the energy stored in a SC and a standard capacitor, with respect to voltage and ratio between the energy stored in a SC and a standard capacitor.

The number of series cells N_s, parallel cells N_p and the total number of cells N_{tot} are calculated with (12)–(14).

$$N_s = \frac{V_{bus}}{V_{cell,M}}, \quad (12)$$

$$N_p = max\left(\frac{E_{cycle}/E_{cell}}{N_s}, \frac{I_{cycle,M}}{I_{cell,M,}}\right) \quad (13)$$

$$N_{tot} = N_s \cdot N_p. \quad (14)$$

in which V_{bus} is the rated voltage chosen for the system. The maximum SC bank current is then obtained as the product of the cell maximum current and the number of parallel cells.

2.2.2. WPT System Design

The chosen resonant IPT system is based on the inductive coupling between two coils in resonance with a compensation network at a given frequency. Among the different antenna architectures, the Double D (DD) topology is chosen because of the high tolerances to misalignment and for the reduced edge effects [23]. As for the compensation network, a series–series (SS) compensation is chosen to avoid the dependence of the mutual inductance on the resonant operating frequency [24,25]. In addition, it offers a wider operating range due to the resonant circuit being less sensitive to variations in the coupling coefficient between the transmitter and receiver coils. This is beneficial for scenarios where perfect alignment might be difficult. In order to correctly design the coupling coils, the bifurcation phenomenon has been considered. This refers to a condition for which the resonance frequency ensuring a Zero Phase Angle (ZPA) between voltage and current at the input terminals, to maximize the power transfer, is not unique [26]. The number of resonance frequencies depends principally on the mutual inductance value, on the load conditions, on the compensation topology and on the self-inductance value of the coils [27]. In particular, for a SS-compensated IPT system, the bifurcation-free condition is realized if the quality factor of the primary side Q_p is greater than a coefficient K_c, depending on the secondary quality factor Q_s. In particular,

$$Q_p = \frac{R_L L_P}{2\pi f M^2}, \qquad Q_s = \frac{2\pi f L_S}{R_L}, \tag{15}$$

$$K_c = \frac{4Q_s^3}{4Q_s^2 - 1}, \tag{16}$$

in which L_P and L_S are, respectively, the primary and the secondary side self-inductance values, M is the mutual inductance value, f is the operating frequency and R_L is the load resistance value. Using the First Harmonic Approximation (FHA) to consider the presence of the rectifier interposed between the inductive coupling and the load, R_L can be obtained as follows:

$$R_L = \frac{8}{\pi^2}\frac{V_{sc}}{I_{sc}}, \tag{17}$$

in which I_{sc} is the charging current and V_{sc} is the charging voltage. The SC bank is charged with a constant current from a minimum voltage $V_{sc,m}$ to a maximum voltage $V_{sc,M}$. Then, the value of R_L is calculated by taking into account the mean value of the SC bank voltage in a charging cycle. Imposing $L_S = L_P = L$, the bifurcation-free condition can then be expressed as in (18).

$$M^2 < \frac{1}{k_f^2} - \frac{1}{4k_f^4 L^2} \quad \text{with} \quad k_f = \frac{2\pi f_R}{R_L}. \tag{18}$$

This condition is given as an input to an iterative MATLAB 2019b algorithm , whose flowchart is shown in Figure 8, together with the coil wire section s_c, the minimum space between turns $d_{t,min}$, the desired dimensions l_c and w_c, and the desired gap g_c between the transmitter and receiver. The outputs of the algorithm are the number of turns N_t, the effective space between turns d_t and finally the self-inductance and mutual inductance values. Thanks to the principle of superposition, both transmitter and receiver coils can be considered as a set of N linear conductors linked by a continuity constrain. For this reason, L and M can be calculated as in (19).

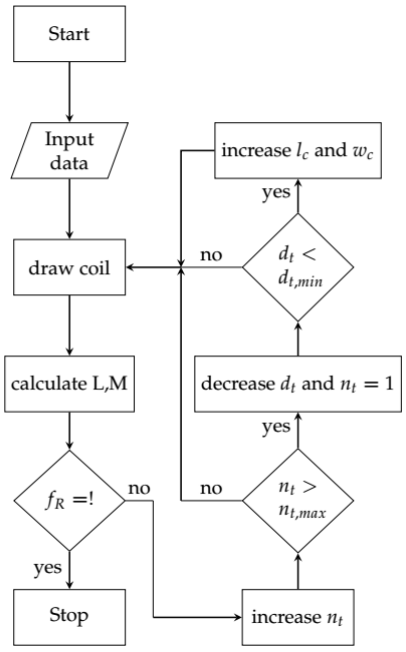

Figure 8. Coil design algorithm flowchart.

$$L \quad (\text{or } M) = \frac{\mu}{I}\sum_{i,j=1}^{N} iV_{i,j}, \tag{19}$$

in which μ is the magnetic permeability, I is a reference current and the $iV_{i,j}$ are the potential vectors induced by the i-th elements on the j-th elements composing the coil for the self-inductance evaluation, or the potential vectors induced by the i-th elements composing the transmitter on the j-th elements composing the receiver in the case of the mutual inductance calculation.

Therefore, the compensation network capacitance for both primary and secondary side is calculated as follows:

$$C_P = C_S = \frac{1}{4\pi^2 f_R^2 L}. \tag{20}$$

3. Simulations

3.1. System-Level Simulation

In order to verify and to assess the performances of the system, a system-level simulation has been carried out in Simulink.

The power profile described in Section 2.1 was scaled down by a factor equal to 3.6×10^{-3}, to be able to carry out validations on a laboratory prototype, considering the available equipment. The maximum allowable powers are 250 W for the charging process, 250 W for discharging and 120 W for regenerative breaking.

The simulation consists of the repetition of six charge–discharge cycles, to emulate six complete bus loop routes. A complete charge–discharge cycle can be divided into two stages, described as follows.

- **Stage 1: Constant Current Charging**. The SC bank is initially charged by the FC through the IPT system with a constant current of 2 A until it reaches its maximum voltage of 48 V. This stage emulate the vehicle charging at the main bus terminal.
- **Stage 2: Discharge**. Once the maximum voltage is achieved, the charging system is deactivated. The SC bank is then connected to the load, represented by the vehicle power demand profile. This configuration emulates a scaled-down power profile that the SC bank would experience in real-world operation.

The simulation results are presented in Section 4, directly compared with the experimental results.

In the system-level simulation, the FC was modeled using the datasheet characteristics, in particular the Voltage-Current (V-I) and the Power-Current (P-I) characteristics.

The boost converter, the primary H-bridge inverter, the magnetic coupling and the secondary rectifier bridge are modeled considering the equality between input and output power, barring an assumed efficiency.

The SC bank was modeled using the three-branches model [28,29], which is adequate for the simulation of the behavior of SCs in the range from seconds to hours.

Finally, the vehicle was simulated using the scaled down power profile.

In the following subsections each block of the system-level simulation is described in detail.

3.1.1. Fuel Cell

The FC used for the small-scale prototype has the characteristics reported in Table 4. The V-I and P-I curves, extracted from the datasheet, are represented in Figure 9.

Using the available data, a simple FC model was implemented. Considering as input the DC/DC boost converter output power, P_{dc}, the FC power can be obtained as follows:

$$P_{fc} = \frac{P_{dc}}{\eta_{dc}}, \tag{21}$$

where $\eta_{dc} = 0.98$ is the DC/DC converter efficiency.

Table 4. Fuel cell datasheet specifications.

Type	Proton Exchange Membrane (PEM)	
Brand	Horizon Fuel Cell	
Specification	Unit	Value
Number of cells	-	72
Nominal power	W	300
Rated voltage	V	43.2
Rated current	A	7.2
Voltage range	V	39–69
H_2 consumption *	L/min	4.2

* At nominal power.

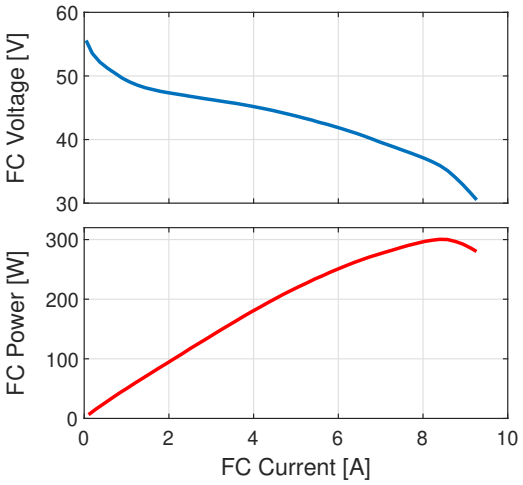

Figure 9. Fuel cell V-I and P-I characteristics.

The FC current I_{fc} can be estimated from the P-I curve. Afterwards, the FC voltage V_{fc} can be obtained from the V-I characteristic. The Simulink block diagram for the FC model is depicted in Figure 10.

The hydrogen consumption is defined for the system operating at nominal power. In order to estimate the hydrogen consumption for different power ratings, a linear dependency was considered.

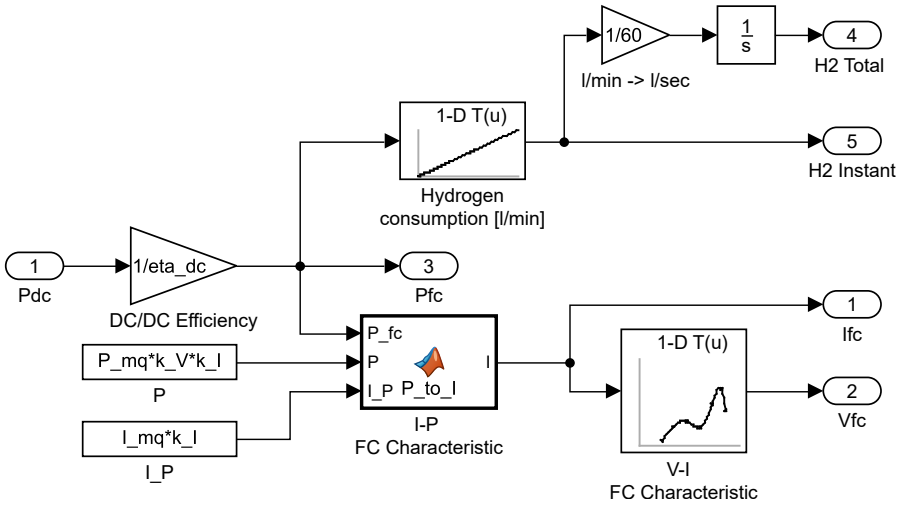

Figure 10. FC Simulink model.

3.1.2. IPT

The IPT system, composed of the primary DC/AC inverter, the magnetic coupling and the AC/DC rectifier, was modeled considering the input/output power equality and assuming an efficiency for the system of $\eta_{ipt} = 0.9$. With the above, the current I_{dc} can be obtained as

$$I_{dc} = \frac{I_{sc} \cdot V_{sc}}{V_{dc} \cdot \eta_{ipt}}. \tag{22}$$

3.1.3. Supercapacitor

The SC bank used for the small-scale prototype is composed of VinaTech SCs whose characteristics are reported in Table 5. As already mentioned, the three-branches model, represented in Figure 11, was chosen, given its ability to simulate the SC behavior even over the long term. In order to characterize the model, a parameter estimation procedure needed to be performed on the experimental voltage response of the SC. This procedure was already performed by the authors in a previous work [30]. The resulting model parameters are reported in Table 6. A pre-assembled SC bank composed of $N_s = 24$, $N_p = 2$ is considered.

Table 5. Supercapacitor datasheet specifications.

Specification	Unit	Value
Rated voltage	V	2.7
Rated capacitance	F	100
AC impedance (1 kHz)	mΩ	6
DC resistance	mΩ	10
Maximum current	A	65
Leakage current	mA	0.2
Stored energy	J	364.5

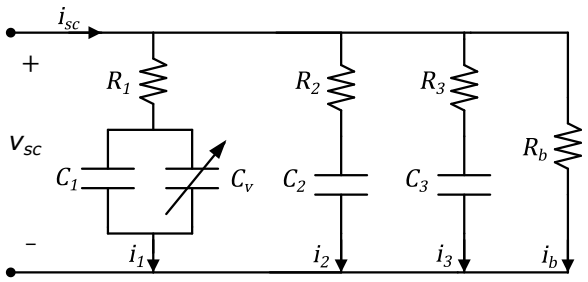

Figure 11. Three-branches equivalent circuit model.

Table 6. Optimized parameters for the SC three-branches model.

R_1 (mΩ)	R_2 (Ω)	R_3 (Ω)	C_1 (F)	C_v (F/V)	C_2 (F)	C_3 (F)
13.2	2.02	28.2	76.5	22.3	69.0	64.7

The voltage across the first branch can be expressed as follows:

$$V_{C_1} = \frac{v_{sc}}{N_s} - i_1 R_1, \tag{23}$$

and the current through the first branch can be formulated as follows:

$$i_1 = \left(C_1 + C_v V_{C_1}\right) \frac{dV_{C_1}}{dt}. \tag{24}$$

From (23) and (24), the SC bank terminal voltage can be obtained as follows:

$$v_{sc} = N_s \left(\int \frac{i_1}{(C_1 + K_V V_{C_1})} dt + i_1 R_1 \right). \tag{25}$$

For the second and third branches, the voltage across the capacitor and the branch current can be expressed as follows:

$$V_{C_{2,3}} = \frac{v_{sc}}{N_s} - i_{2,3} R_{2,3}, \tag{26}$$

$$i_{2,3} = \frac{1}{R_{2,3}} \left(\frac{v_{sc}}{N_s} - V_{C_{2,3}} \right). \tag{27}$$

The total SC bank current is as follows:

$$i_{sc} = N_p \left(i_1 + i_2 + i_3 + \frac{v_{sc}}{R_{dis}} \right). \tag{28}$$

From (28), the current on the first branch can be expressed as follows:

$$i_1 = \frac{i_{sc}}{N_p} - \left(i_2 + i_3 + \frac{v_{sc}}{R_{dis}} \right). \tag{29}$$

Equations (23)–(29) were implemented in Simulink with the block diagram shown in Figure 12.

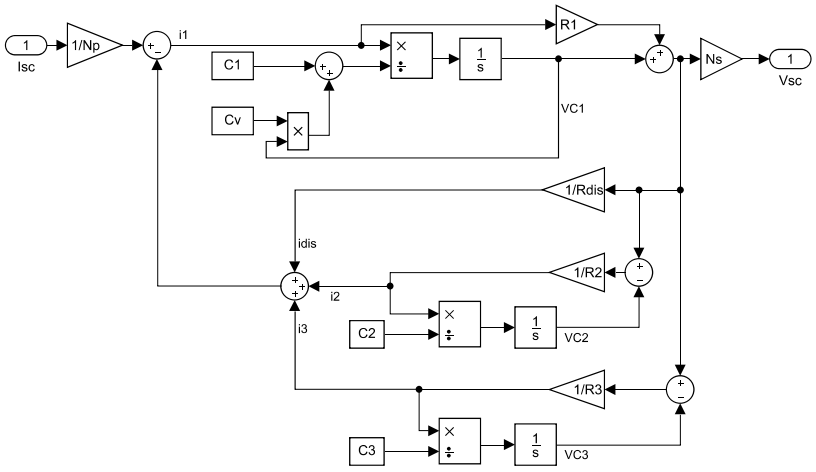

Figure 12. Simulink implementation of the three-branches model.

3.1.4. Discharge Profile

When the charging process is completed, the SC bank is disconnected from the charging station and the simulation of the driving cycle starts. The power at time t_i is divided by the SC voltage at time t_i to obtain the SC current at time t_{i+1}.

$$i_{sc}(t_{i+1}) = \frac{P_{sc}(t_i)}{V_{sc}(t_i)} \tag{30}$$

3.2. Hardware-Level Simulation

The system-level simulation does not allow verification of all the performances of the system. In particular, the real operation of the power electronics converters, of the magnetic coupling and of the control system need to be evaluated. Figure 13 shows the detailed schematic of the system, simulated in PLECS 4.8.1.

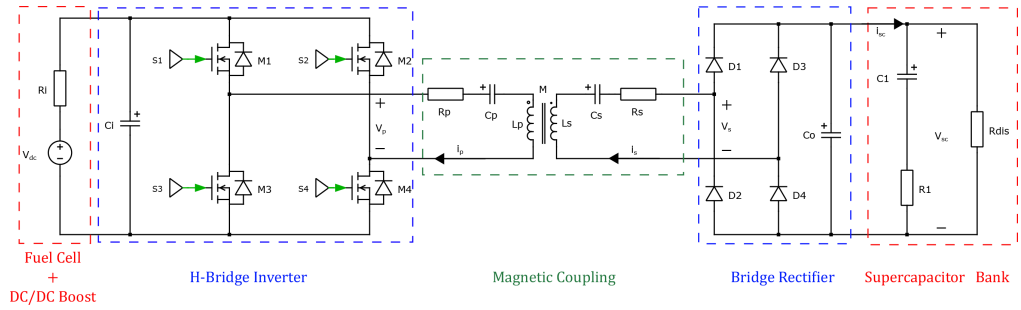

Figure 13. PLECS schematic for the hardware-level simulation.

3.2.1. Fuel Cell

To simplify the hardware-level simulation, the FC and the DC/DC boost converter were replaced with a constant voltage source $V_{dc} = 48$ V.

3.2.2. IPT

By applying the criterion described in Section 2.2.2, the DD coupling coils have been designed considering an operating resonant frequency $f_R = 100$ kHz. They are shown in Figure 14 and their characteristics are reported in Table 7. As it can be noticed in Figure 15, the imaginary part of the total input impedance Z_T is equal to zero at $f = f_R$ to perform the ZPA and the chosen resonant frequency is unique, as it can be observed by the comparison between Q_p and K_c. The capacitance value of the compensation network is calculated as in (20) and it is equal to $C_p = C_s = 42.09$ nF. The internal resistances of the primary side coil R_p and secondary side coil R_s are equal to 0.41 Ω.

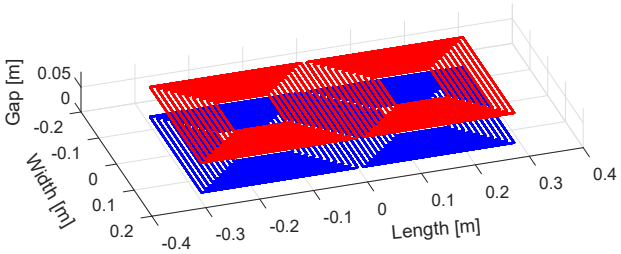

Figure 14. Designed DD coils: transmitter (blue) and receiver (red).

Table 7. Coil characteristics.

l_c [cm]	w_c [cm]	g_c [cm]	d_t [cm]	s_c [mm^2]	N_t [−]	L [µH]	M [µH]
58	29	6	1	2.5	10	60.18	23

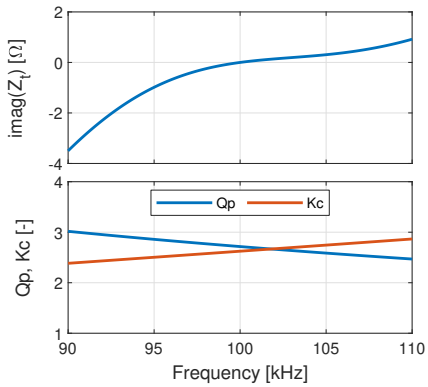

Figure 15. Input total impedance trend and comparison between Q_p and K_c, with respect to frequency.

3.2.3. Supercapacitor

The SC bank, in this case, can be modeled as an ideal capacitor with an Equivalent Series Resistor (ESR) and a parallel resistor. In fact, since the time of simulation is in the order of seconds, the voltage-dependent capacitor, the second and the third branches do not have influence on the SC voltage response and can be neglected.

3.2.4. Power Electronics and Control

The first harmonic of the inverter output voltage $v_{p,1}$ and the output current I_o, considering a Phase Shift Modulation control, can be expressed as follows:

$$v_{p,1} = \frac{4V_{DC}}{\pi} \cos\left(\frac{\pi}{2}D\right) \sin(\omega_0 t), \qquad I_o = \frac{8}{\omega_0 M} \frac{V_{in}}{\pi^2} \cos\left(\frac{\pi}{2}D\right), \tag{31}$$

where D is the duty cycle. From (31), it can be deduced that the SC bank charging current can be regulated varying the duty cycle of the H-bridge inverter. Subsequently, a closed-loop control was implemented in the simulation. The SC bank current is compared to the desired charging current and the error is sent to a Proportional–Integral (PI) controller. The PI controller processes the error and returns the value for the duty cycle, as shown in Figure 16a. Using the Routh–Hurwitz stability criterion, the PI regulator parameters are chosen as $K_p = 0.05$ and $K_i = 1000$. Figure 16b shows the SC voltage and current, and the H-bridge inverter duty cycle. The SC charging current is initially set to 2 A. At $t = 25$ ms, a step change to the SC charging current from 2 A to 2.5 A is given in order to verify the control performances. It can be noticed that the controller reacts with a settling time lower than 1.5 ms. At $t = 50$ ms, the SC charging current is again set to 2 A.

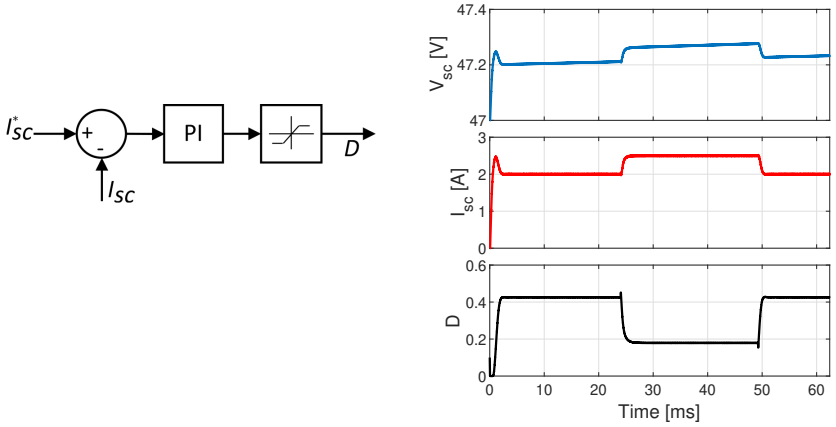

(**a**) (**b**)

Figure 16. Closed-loop control: (**a**) block diagram, (**b**) test waveform.

4. Experimental Validation

An experimental test was performed on the scaled-down prototype to validate the simulation results. The test bench is shown in Figure 17. All the employed components are listed in Table 8.

The performed test was carried out following the same approach as the system-level simulation. The SC bank was firstly charged at a constant current (2 A) up to the maximum voltage (48 V) by the system composed of the FC and the IPT.

Once the maximum voltage was reached, the charging system was disabled and the SC bank was connected to the parallel between the electronic load and the generator to emulate the scaled-down power profile.

When the cycle was finished (the bus completed its loop route), the SC bank was reconnected to the FC and IPT system, to be recharged again at a constant current.

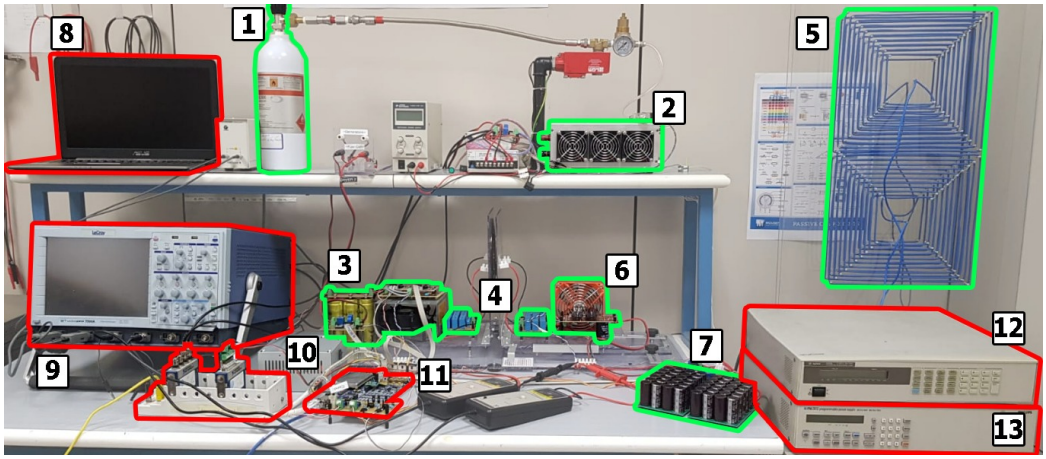

Figure 17. Test bench setup: 1. hydrogen tank, 2. fuel cell, 3. primary side converter, 4. compensation capacitances, 5. IPT coils, 6. secondary side converter, 7. supercapacitor bank, 8. control computer, 9. oscilloscope, 10. acquisition board, 11. PED board, 12. electronic load, 13. power supply.

Table 8. Test bench components.

Figure 17 Ref.	Component	Characteristics
	HYDROGEN-BASED POWER SUPPLY	
1.	H2PLANET Hydrogen tank	900 L metal hydride P = 10 bar
2.	H2PLANET PEM fuel cell	see Table 4
	IPT SYSTEM	
3.	Primary side H-bridge inverter	C_i = 10 mF input capacitor IRFB4115 Power MOSFET IR2110 drivers
4.	Compensation networks	see Section 3.2.2
5.	Coupling coils	see Table 7
6.	Bridge rectifier	MUR3020WTG diodes C_o = 2 mF output capacitor
	SUPERCAPACITOR	
7.	Supercapacitor bank	see Section 3.1.3
	CONTROL AND ACQUISITION	
8.	PC	control panel
9.	Oscilloscope	Lecroy WavePro 7200A
10.	Acquisition board	NI 9215 16-Bit
11.	Control system	PED Board [31]
12.	Electronic load	Agilent 6060B 3–60 V/0–60 A, 300 W
13.	Power supply	Fluke PM2812 0–60 V/0–10 A, 120 W

The cycle was repeated six times. The duration of the discharge cycle was 967 s. The duration of the charge varied depending on the voltage to which the SC bank was brought at the end of each discharge cycle. The results of experimental tests are presented below, compared to the system-level and hardware-level simulation results. In particular, Figure 18 shows the comparison of simulation (a) and experimental (b) results. From the top to the bottom of Figure 18a,b, the FC voltage V_{fc} and current I_{fc}, the DC-link voltage

V_{dc} and current I_{dc}, the SC voltage V_{sc} and current I_{sc}, and the efficiency η are shown. The last graph of Figure 18a shows the estimated hydrogen consumption, while Figure 18b shows the inverter duty cycle trend.

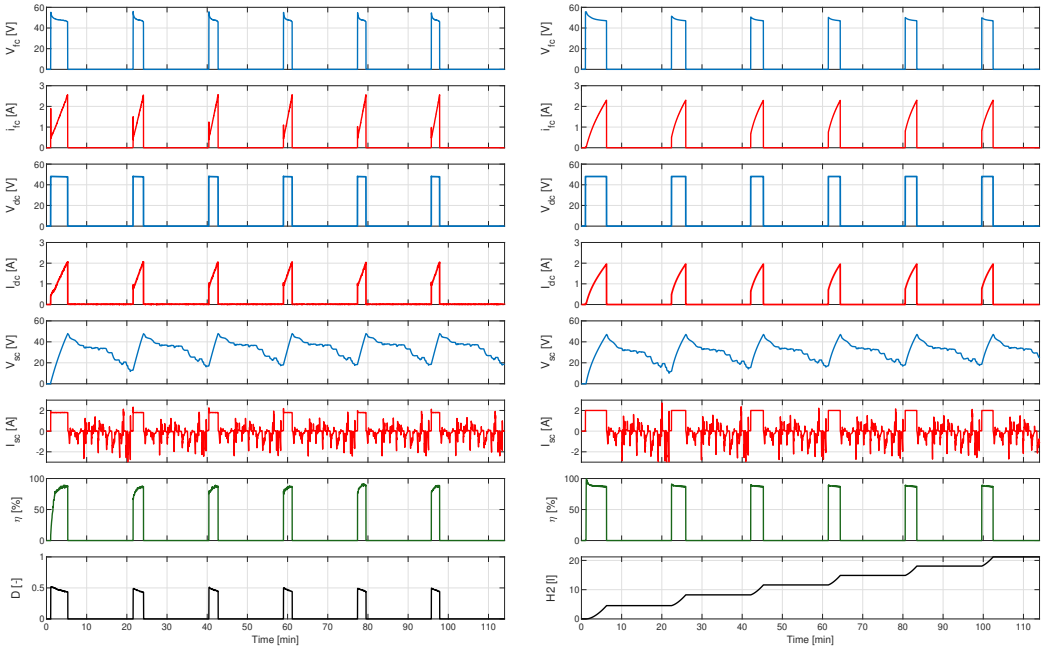

(**a**) (**b**)

Figure 18. System level: (**a**) Simulation results. (**b**) Experimental results.

The experimental test results demonstrate a remarkable degree of similarity between the observed waveforms and those predicted by the system-level simulation, even considering the necessary approximations made during the modeling process. This high level of agreement underscores the validity of the chosen approach.

A closer examination of the experimental data reveals that, due to the inherent response characteristics of the actual supercapacitor (SC) bank, its voltage exhibits a gradual increase at the conclusion of each cycle. This trend stabilizes after a few cycles, reaching a steady state. The simulation replicates this phenomenon, providing further validation for the three-branch model employed to represent the behavior of the SC bank.

However, when focusing on efficiency metrics, some deviations between the simulated and experimental results become apparent. These discrepancies can be attributed to the simplifying assumptions made during the system-level simulation. For instance, the simulation assumes constant efficiencies for both the DC/DC converter and the Inductive Power Transfer (IPT) systems. In reality, the efficiency of these systems is demonstrably influenced by the load, which inherently fluctuates in practical applications.

Figure 19 shows the comparison between the hardware-level simulation and the experimental waveforms. In particular, Figure 19a,b show, respectively, the simulation and the experimental inverter output voltage v_p and current i_p. Figure 19c,d show respectively the simulation and the experimental rectifier input voltage v_s and current i_s. The close correspondence between the simulated and experimental waveforms serves as a powerful validation of the design methodology employed for the Inductive Power Transfer (IPT) system. As can be observed, the system is not in perfect resonance. This is due to the fact that the capacitors used for the compensation network in the real prototype do not have an exact capacitance of 42.09 nF, as calculated, but rather 40 nF (the real capacitance value was also used in the simulations). In general, the high degree of agreement underscores the effectiveness of the modeling approach in accurately capturing the system behavior. This successful validation instills confidence in the IPT system design. It suggests that the

system will perform as intended when implemented in real-world applications, achieving the desired level of power transfer efficiency.

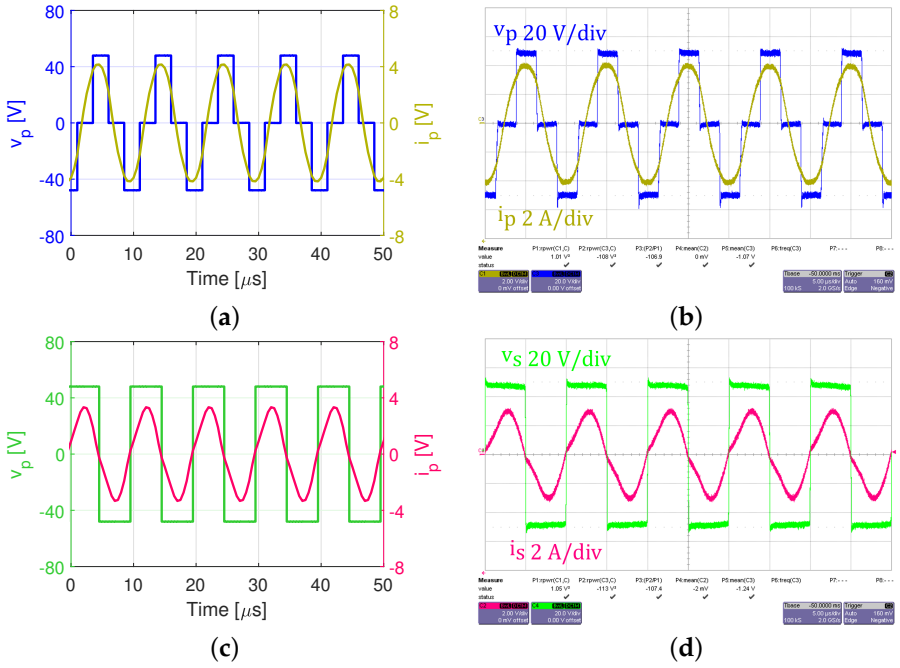

Figure 19. Hardware level: (**a**) Primary side simulated waveforms. (**b**) Primary side experimental waveforms. (**c**) Secondary side simulated waveforms. (**d**) Secondary side experimental waveforms.

5. Technical–Economical Analysis

The experimental validation of the scaled prototype confirms the possibility of using this type of system for public transportation; then, a technical–economical analysis taking into account the real power level is carried out. The SC supply system is compared to a traditional Li-ion battery supply system. The shuttle bus charging–discharging cycle parameters taken into account for the analysis are shown in Table 9. It should be noticed that the SCs are sized to be recharged every time the bus stops at the terminal station, while the batteries are sized to be recharged once per day. In particular, considering a charging standard of 22 kW, the time for the stop at the main terminal is less than 4 min, and it is therefore considered acceptable for the normal operation of the transport system. Charging power can be increased to reduce the charging time; however, the cost of the charging infrastructure would increase as well.

Table 9. Cycle parameters.

	Supercapacitors	**Batteries**
charges/day	20	1
days/week	5	5
weeks/year	50	50
cycles/year	5000	250
V_{bus} [V]	400	400
E_{cycle} [kWh]	1.4	39.2 (*)
$I_{cycle_{max}}$ [A]	113.75	113.75

(*) Forty percent of depth of discharge.

Five different commercial VinaTech and Maxwell SCs were considered, whose characteristics are reported in Table 10.

Table 10. Supercapacitor characteristics.

SC	1	2	3	4	5	
C	500	360	500	800	3000	F
$V_{cell,M}$	3	2.7	2.7	2.3	3	V
ESR	3.2	4.5	4.5	15	0.26	mΩ
$I_{cell,M}$	283	185	205	12.5	2200	A
E_{cell}	0.78	0.45	0.63	0.73	4.66	Wh
Weight	0.08	0.07	0.096	0.0945	0.525	kg
Volume	69.2	59.6	78.9	69.2	390.19	mL
Life cycles	5×10^5	1×10^5	1×10^5	1×10^5	1×10^6	-

By applying the design criterion reported in Section 2.2.1, the calculated SC bank parameters are reported in Table 11.

Table 11. SC bank design parameters.

SC	1	2	3	4	5
N_s	133	148	148	174	133
N_p	14	21	16	12	3
N_{tot}	1867	3111	2370	2087	400
Max Current [A]	4032	3885	3280	150	6600

For the battery pack, two different commercial Sanyo and Sony Li-ion cells were considered, whose characteristics are shown in Table 12.

Table 12. Battery characteristics.

Battery	1	2	
C	2.6	3.45	Ah
$V_{cell,r}$	3.6	3.6	V
ESR	100	96	mΩ
$I_{cell,M}$	5	5	A
E_{cell}	9.36	12.42	Wh
Weight	0.048	0.048	kg
Volume	16.54	16.54	mL
Life cycles (*)	1500	1500	-

(*) Forty percent of depth of discharge.

The battery cell energy E_{cell} is calculated as the product of the battery capacity C and the battery cell rated voltage $V_{cell,r}$. The number of series cells N_s, parallel cells N_p and the total number of cells N_{tot} are calculated as in (12), (13) and (14). Their values are reported in Table 13.

Table 13. Battery pack design parameters.

Battery	1	2
N_s	111	111
N_p	46	33
N_{tot}	5152	3696
Max current [A]	115	115.5

Weights, volumes, costs and periods of possible service were analyzed for the chosen SC banks and the battery packs. They are summarized in Table 14.

Table 14. SC–battery comparison.

	Weight [kg]	Volume [L]	Cost [EUR]	Possible Service Period [Years]
SC 1	144	124.71	14,028.67	100
SC 2	216.3	184.17	21,217.78	20
SC 3	213.6	175.54	23,703.70	20
SC 4	181.1	132.61	20,869.57	20
SC 5	157.7	117.20	22,000.00	200
Battery 1	274.30	85.22	12,880.00	6
Battery 2	177.41	61.13	12,566.40	6

As can be clearly noted, there is no significant weight difference between the SC banks and the battery packs. The lower volumes of the battery packs are due to their higher energy density.

Another important consideration has to be focused on the safety and thermal management of both technologies. As a matter of fact, supercapacitors typically operate at much lower temperatures than batteries. This is because they store energy through the physical separation of charges, not chemical reactions. Batteries, especially Lithium-ion types, generate heat during charging and discharging due to these internal reactions. Lower operating temperatures in supercapacitors translate to a reduced risk of thermal runaway and no need for complex cooling systems. In addition, unlike Lithium-ion batteries which use flammable electrolytes, supercapacitors typically use safer electrolytes like aqueous solutions or organic solvents with lower flammability. This reduces the risk of fire even in the case of a malfunction. Moreover, to compare the two technologies from an economic standpoint, it is necessary to consider the Total Cost of Ownership (TCO), which encompasses all costs associated with an asset, product or service. TCO can be represented by the following formula:

$$TCO = C_a + C_o + C_{EoL}. \tag{32}$$

C_a is the acquisition cost and it includes the initial purchase price of the asset. In Table 14, the acquisition costs are calculated as the product of the cost per single cell and the total number of cells. As can be observed, the acquisition cost of batteries is lower than that of SCs. C_o is the operating cost. It represents the ongoing expenses incurred during the asset operational life. In this case, a significant factor influencing operating costs is the lifespan of the batteries and SCs. While batteries have a lower initial cost, they may require multiple replacements throughout the vehicle lifespan, typically 20 years. This can lead to higher overall operating costs for batteries compared to SCs, which have a longer lifespan and may not require replacement during the vehicle lifetime. C_{EoL} is the end-of-life cost and it refers to the costs associated with the proper disposal of the asset at the end of its useful life. These costs may include recycling or special treatment procedures. By considering all three components of TCO, a more comprehensive assessment of the economic viability of batteries and supercapacitors can be achieved. While batteries may have a lower initial acquisition cost, their higher operating costs due to frequent replacements and potential end-of-life disposal costs could make supercapacitors a more cost-effective solution in the long run.

6. Conclusions

This article delves into a pioneering urban transportation system that leverages the combined power of supercapacitors (SCs) and a fuel cell (FC)-powered wireless charging system for electric buses. The proposed system represents a significant leap forward in sustainable public transportation. First, a comprehensive design was created, encompassing both the system and its hardware components. This design was then evaluated through simulations at both the system and hardware levels.

To validate the theoretical framework, a scaled-down prototype was meticulously constructed and subjected to a series of controlled experiments. The design process, jointly to the experimental validation revealed the following:

- Fuel cells and the use of hydrogen offer an excellent solution for powering the charging system. This is because the charging occurs at constant power, so, even though the fuel cell is a low-dynamic system, it is well suited for this application. Additionally, fuel cells can help compensate for the variability in renewable energy sources.
- Employing a wireless charging system offers several advantages, primarily due to the absence of physical connections. In particular, it is crucial to consider the bifurcation phenomenon during the design of such systems. Additionally, implementing a series–series compensation scheme ensures that the mutual inductance remains independent of the load, thereby achieving resonance conditions regardless of any misalignment or capacitor charge state.
- While supercapacitors may not be suitable for vehicles requiring long ranges, they prove particularly advantageous in applications involving shorter routes, such as public transportation buses. This aligns with the growing recognition of supercapacitor viability for such applications.

Beyond the technical aspects, this article delves into the economic viability of the SC-based system. A simple economic analysis was conducted to compare the cost-effectiveness of this approach against the traditional, battery-powered alternative. This analysis employed real-world data, specifically the power and energy demands of a shuttle bus operating within a real scenario. The analysis revealed a significant advantage for the SC-based system. The long-term storage system cost associated with the SC approach is demonstrably lower compared to the traditional battery-based system. This economic advantage positions SCs as a highly attractive solution for sustainable urban transportation. Despite the advantages shown in this work, additional analysis has to be conducted to prove the feasibility of such a system. As a future development, an overall energy utilization efficiency analysis will be performed, together with the implementation of a full-scale system, acting as a living laboratory.

Author Contributions: Conceptualization, N.C., V.C. and R.M.; Methodology, N.C. and V.C.; Investigation, N.C. and V.C.; Data curation, N.C.; Writing—original draft, N.C.; Writing—review & editing, F.G.; Supervision, A.A.M.; Funding acquisition, R.M. and A.A.M. All authors have read and agreed to the published version of the manuscript.

Funding: This research has been partially supported by the European Union—NextGenerationEU—National Sustainable Mobility Center CN00000023, Italian Ministry of University and Research Decree n. 1033—17/06/2022, Spoke 3, CUP B73C22000760001, by the project 'SiciliAn MicronanOTecH Research And Innovation CEnter' 'SAMOTHRACE' (MUR, PNRR-M4C2, ECS-00000022), spoke 3—Università degli Studi di Palermo 'S2-COMMs'—Micro and Nanotechnologies for Smart & Sustainable Communities", by the project "Network 4 Energy Sustainable Transition—NEST", CUP B73C22001280006, Project code PE0000021, Concession Decree No. 1561 of 11.10.202, by the OPTEBUS project (Development of an Optimal Design Tool for Electrification of Urban Public Transportation BUS Services)—PRIN Progetti di Rilevante Interesse Nazionale 2022-PRJ-0969—ID 42740, by the ESPFET project (Enhanced Energy-Saving Powertrains for Freight E-Transportation)—PRIN Progetti di Rilevante Interesse Nazionale 2022-PRJ-0962—ID 42679 and European Project ECS4DRES (Electronic Components and Systems for flexible, coordinated and resilient Distributed Renewable Energy Systems). The project has received funding from Key Digital Technologies (KDT) under grant agreement no. 101139790.

Data Availability Statement: The original contributions presented in the study are included in the article, further inquiries can be directed to the corresponding author.

Conflicts of Interest: Authors Francesco Gennaro and Angelo Messina were employed by the company ST Microelectronics. The remaining authors declare that the research was conducted in the absence of any commercial or financial relationships that could be construed as a potential conflict of interest.

References

1. IEA. CO_2 Emissions in 2022, 2022 Highlights. International Energy Agency Report. 2023. Available online: https://www.iea.org.
2. Khaligh, A.; Li, Z. Battery, Ultracapacitor, Fuel Cell, and Hybrid Energy Storage Systems for Electric, Hybrid Electric, Fuel Cell, and Plug-In Hybrid Electric Vehicles: State of the Art. *IEEE Trans. Veh. Technol.* **2010**, *59*, 2806–2814. [CrossRef]
3. Gu, Y.; Liu, M. Fair and Privacy-Aware EV Discharging Strategy Using Decentralized Whale Optimization Algorithm for Minimizing Cost of EVs and the EV Aggregator. *IEEE Syst. J.* **2021**, *15*, 5571–5582. [CrossRef]
4. Chau, M.L.Y.; Koutsompina, D.; Gkiotsalitis, K. The Electric Vehicle Scheduling Problem for Buses in Networks with Multi-Port Charging Stations. *Sustainability* **2024**, *16*, 1305. [CrossRef]
5. Berrueta, A.; Ursua, A.; Martin, I.S.; Eftekhari, A.; Sanchis, P. Supercapacitors: Electrical Characteristics, Modeling, Applications, and Future Trends. *IEEE Access* **2019**, *7*, 50869–50896. [CrossRef]
6. Wei, L.; Wu, M.; Yan, M.; Liu, S.; Cao, Q.; Wang, H. A Review on Electrothermal Modeling of Supercapacitors for Energy Storage Applications. *IEEE J. Emerg. Sel. Top. Power Electron.* **2019**, *7*, 1677–1690. [CrossRef]
7. Zhou, J.; Zhao, J.; Wang, L. Cost-Based Research on Energy Management Strategy of Electric Vehicles Using Hybird Energy Storage System. *Tsinghua Sci. Technol.* **2024**, *29*, 684–697. [CrossRef]
8. Sidharthan, V.P.; Kashyap, Y.; Kosmopoulos, P. Adaptive-Energy-Sharing-Based Energy Management Strategy of Hybrid Sources in Electric Vehicles. *Energies* **2023**, *16*, 1214. [CrossRef]
9. Zhang, Y.; Liu, J.; Cui, S.; Zhou, M. Parameter Matching Methods for Li Battery–Supercapacitor Hybrid Energy Storage Systems in Electric Buses. *Machines* **2022**, *10*, 85. [CrossRef]
10. Muralidharan, V.; Narayanan, R.; Nithish, J.; Febin daya, J.L. A Novel Supercapacitor Assisted Regenerative Braking Scheme for Electric Vehicle. In Proceedings of the 2022 International Virtual Conference on Power Engineering Computing and Control: Developments in Electric Vehicles and Energy Sector for Sustainable Future (PECCON), Chennai, India, 5–6 May 2022; pp. 1–7. [CrossRef]
11. Yilmaz, M.; Krein, P.T. Review of Battery Charger Topologies, Charging Power Levels, and Infrastructure for Plug-In Electric and Hybrid Vehicles. *IEEE Trans. Power Electron.* **2013**, *28*, 2151–2169. [CrossRef]
12. Zhang, Z.; Pang, H.; Georgiadis, A.; Cecati, C. Wireless Power Transfer—An Overview. *IEEE Trans. Ind. Electron.* **2019**, *66*, 1044–1058. [CrossRef]
13. Ramakrishnan, V.; Dominic, S.A.; Balaji, C.; Rajamanickam, N.; Kotb, H.; Elrashidi, A.; Nureldeen, W. A Comprehensive Review on Efficiency Enhancement of Wireless Charging System for the Electric Vehicles Applications. *IEEE Access* **2024**, *12*, 46967–46994. [CrossRef]
14. Mahesh, A.; Chokkalingam, B.; Mihet-Popa, L. Inductive Wireless Power Transfer Charging for Electric Vehicles—A Review. *IEEE Access* **2021**, *9*, 137667–137713. [CrossRef]
15. Shevchenko, V.; Pakhaliuk, B.; Husev, O.; Vinnikov, D.; Strzelecki, R. Wireless Charging Station Design for Electric Scooters: Case Study Analysis. *Energies* **2024**, *17*, 2472. [CrossRef]
16. ElGhanam, E.; Sharf, H.; Odeh, Y.; Hassan, M.S.; Osman, A.H. On the Coordination of Charging Demand of Electric Vehicles in a Network of Dynamic Wireless Charging Systems. *IEEE Access* **2022**, *10*, 62879–62892. [CrossRef]
17. Bensetti, M.; Kadem, K.; Pei, Y.; Le Bihan, Y.; Labouré, E.; Pichon, L. Parametric Optimization of Ferrite Structure Used for Dynamic Wireless Power Transfer for 3 kW Electric Vehicle. *Energies* **2023**, *16*, 5439. [CrossRef]
18. Shi, W.; Dong, J.; Soeiro, T.B.; Bauer, P. Integrated Solution for Electric Vehicle and Foreign Object Detection in the Application of Dynamic Inductive Power Transfer. *IEEE Trans. Veh. Technol.* **2021**, *70*, 11365–11377. [CrossRef]
19. Shi, W.; Grazian, F.; Dong, J.; Soeiro, T.B.; Bauer, P. Detection of Metallic Foreign Objects and Electric Vehicles Using Auxiliary Coil Sets for Dynamic Inductive Power Transfer Systems. In Proceedings of the 2020 IEEE 29th International Symposium on Industrial Electronics (ISIE), Delft, The Netherlands, 17–19 June 2020; pp. 1599–1604. [CrossRef]
20. Bertoluzzo, M.; Di Barba, P.; Forzan, M.; Mognaschi, M.E.; Sieni, E. A Deep Learning Approach to Improve the Control of Dynamic Wireless Power Transfer Systems. *Energies* **2023**, *16*, 7865. [CrossRef]
21. Feng, C.; Shao, C.; Xiao, Y.; Dong, Z.; Wang, X. Day-Ahead Strategic Operation of Hydrogen Energy Service Providers. *IEEE Trans. Smart Grid* **2022**, *13*, 3493–3507. [CrossRef]
22. Tavakoli, S.D.; Dozein, M.G.; Lacerda, V.A.; Mañe, M.C.; Prieto-Araujo, E.; Mancarella, P.; Gomis-Bellmunt, O. Grid-Forming Services From Hydrogen Electrolyzers. *IEEE Trans. Sustain. Energy* **2023**, *14*, 2205–2219. [CrossRef]
23. Bima, M.E.; Bhattacharya, I.; Adepoju, W.O.; Banik, T. Effect of Coil Parameters on Layered DD Coil for Efficient Wireless Power Transfer. *IEEE Lett. Electromagn. Compat. Pract. Appl.* **2021**, *3*, 56–60. [CrossRef]
24. Wu, M.; Yang, X.; Cui, H.; Chen, W.; Wang, L.; Zhu, L.; Yu, X.; Yan, Z. Modeling of Litz-Wire DD Coil With Ferrite Core for Wireless Power Transfer System. *IEEE Trans. Power Electron.* **2023**, *38*, 6653–6669. [CrossRef]
25. Bima, M.E.; Bhattacharya, I.; Neste, C.W.V. Experimental Evaluation of Layered DD Coil Structure in a Wireless Power Transfer System. *IEEE Trans. Electromagn. Compat.* **2020**, *62*, 1477–1484. [CrossRef]
26. Nguyen, H.T.; Alsawalhi, J.Y.; Hosani, K.A.; Al-Sumaiti, A.S.; Jaafari, K.A.A.; Byon, Y.J.; Moursi, M.S.E. Review Map of Comparative Designs for Wireless High-Power Transfer Systems in EV Applications: Maximum Efficiency, ZPA, and CC/CV Modes at Fixed Resonance Frequency Independent from Coupling Coefficient. *IEEE Trans. Power Electron.* **2022**, *37*, 4857–4876. [CrossRef]

27. Tiwari, P.; Ronanki, D. Bifurcation Free Coil Design for Multi Power Level Wireless Charging of Electric Vehicles. In Proceedings of the 2022 IEEE International Conference on Power Electronics, Drives and Energy Systems (PEDES), Jaipur, India, 14–17 December 2022; pp. 1–6. [CrossRef]
28. Zucca, M.; Hassanzadeh, M.; Conti, O.; Pogliano, U. Accurate Parameters Identification of a Supercapacitor Three-Branch Model. *IEEE Access* **2023**, *11*, 122387–122398. [CrossRef]
29. Castiglia, V.; Campagna, N.; Tommaso, A.O.D.; Miceli, R.; Nevoloso, C.; Pellitteri, F.; Puccio, C.; Viola, F. Modeling, Simulation, and Characterization of a Supercapacitor in Automotive Applications. *IEEE Trans. Ind. Appl.* **2022**, *58*, 2421–2429. [CrossRef]
30. Castiglia, V.; Campagna, N.; Di Tommaso, A.O.; Miceli, R.; Pellitteri, F.; Puccio, C.; Viola, F. Modelling, Simulation and Characterization of a Supercapacitor in Automotive Applications. In Proceedings of the 2020 Fifteenth International Conference on Ecological Vehicles and Renewable Energies (EVER), Monte-Carlo, Monaco, 10–12 September 2020; pp. 1–6. [CrossRef]
31. PED-Board Datasheet. Available online: https://www.ped-board.com.